

# Far ultraviolet airglow remote sensing measurements on Feng Yun 3D meteorological satellite

Yungang Wang<sup>1,2</sup>, Liping Fu<sup>3</sup>, Fang Jiang<sup>3</sup>, Xiuqing Hu<sup>1</sup>, Chengbao Liu<sup>1</sup>, Xiaoxin Zhang<sup>1,2</sup>,  
Jiawei Li<sup>1,2</sup>, Zhipeng Ren<sup>4</sup>, Fei He<sup>4</sup>, Lingfeng Sun<sup>4</sup>, Ling Sun<sup>1</sup>, Zhongdong Yang<sup>1</sup>, Peng Zhang<sup>1</sup>,  
5 Jingsong Wang<sup>1,2</sup>, Tian Mao<sup>1,2</sup>

1 National Satellite Meteorological Center, Chinese Meteorological Administration, Beijing, China

2 Key Laboratory of Space Weather, National Center for Space Weather, Chinese Meteorological Administration, Beijing,  
China

3 National Space Science Center, Chinese Academy of Sciences, Beijing, China

10 4 Key Laboratory of Earth and Planetary Physics, Institute of Geology and Geophysics, Chinese Academy of Sciences,  
Beijing, China

*Correspondence to: Tian Mao (email: maotian@cma.cn)*

**Abstract.** The Ionospheric Photometer (IPM) is carried on the Feng Yun 3D (FY3D) meteorological satellite, which allows  
for the measurement of far-ultraviolet (FUV) airglow radiation in the thermosphere. IPM is a compact and high-sensitivity  
15 nadir-viewing FUV remote sensing instrument. It monitors 135.6 nm emission in the night-side thermosphere and 135.6 nm  
and N<sub>2</sub> LBH emissions in the day-side thermosphere that can be used to invert the peak electron density of the F2 layer  
(NmF<sub>2</sub>) at night and O/N<sub>2</sub> ratio in the daytime, respectively. Preliminary observations show that the IPM could monitor the  
global structure of the equatorial ionization anomaly (EIA) structure around 2:00 local time using OI 135.6 nm nightglow  
~~properly~~. It could also identify the reduction of O/N<sub>2</sub> in the high-latitude region during the geomagnetic storm of Aug. 26,  
20 2018. The IPM derived NmF<sub>2</sub> accords well with that observed by 4 ionosonde stations along 120°E with a standard deviation  
of 26.67%. Initial results demonstrate that the performance of IPM meets the ~~designed~~ requirements and therefore can be  
used to study the thermosphere and ionosphere in the future.

## 1 Introduction

The Earth's far-ultraviolet (FUV) airglow radiation from the thermosphere includes the emission of H, O, and N<sub>2</sub> and the  
25 absorption of O<sub>2</sub> (Meier, 1991). The OI 135.6 nm nightglow emission, which is mainly produced by the recombination of  
ionospheric O<sup>+</sup> and electron, ~~can present~~ represents the spatial and temporal variations of the ionosphere in the nighttime. The  
135.6 nm and N<sub>2</sub> LBH dayglow emission, which are produced by energetic photon-electron impact excitation of the neutral

atmosphere, are used to derive the ~~characteristics of~~ column O/N<sub>2</sub> in the sunlit disk. The ~~FUV radiation can be completely absorbed by the lower atmosphere, and the~~ Earth's atmosphere is opaque to the FUV radiation due to the lower atmosphere absorption. The background emission of FUV airglow from the Earth's surface is absent. So FUV airglow radiation is particularly well-suited to space-based remote sensing (Paxton et al., 2003; Budzien et al., 2019). In past decades, FUV spectrography ~~based on satellites~~ has been used extensively in studying the thermosphere and ionosphere from satellites, such as: GUVI (the Global Ultra-Violet Imager) on the NASA TIMED (Thermosphere, Ionosphere, Mesosphere Energetics and Dynamics) satellite (Christensen et al., 2003); and the Far Ultraviolet Imager (FUV) on the NASA IMAGE (Imager for Magnetopause-to-Aurora Global Exploration) satellite (Sagawa et al., 2005). The other useful ~~equipment-instrument used in studying the thermosphere and ionosphere~~ is ionospheric photometer, which is compact and high-sensitive. The photometer on the polar-orbiting Department of Defense satellite S3-4 was used in measuring of the airglow, aurora, and solar scatter radiance of the earth's atmosphere (Huffman et al., 1980). The U.S. Naval Research Laboratory ~~firstly~~ gave the concept for a new class of ionospheric photometer twenty years ago. It was supplied in the Tiny Ionospheric Photometer (TIP) on the Constellation Observing System for Meteorology, Ionosphere, and Climate satellites (Anthes et al., 2008; Dymond et al., 2016), complemented and upgraded in the Tiny Ionospheric Photometer (TIP) as part of the GPS Radio Occultation and Ultraviolet Photometry –Colocated (GROUP-C) experience on the International Space Station (Budzien et al., 2019; Budzien et al., 2017), and notably improved in the Triple Tiny Ionospheric Photometer (Tri-TIP) in Coordinated Ionospheric Reconstruction CubeSat Experience (Dymond et al., 2017; Stephan et al., 2018).

The compact and high-sensitivity nadir-viewing FUV Ionospheric Photometer (IMP) is one of ten scientific payloads aboard the ~~FY3D-Feng Yun 3D~~ meteorological satellite. IPM monitors 135.6 nm emission in the night-side thermosphere and 135.6 nm and N<sub>2</sub> LBH emissions in the day-side thermosphere by employing a filter wheel that adds two red-leak signal channels for daytime and nighttime red-leak<sub>s</sub> respectively. Red-leak<sub>s</sub> refers to weak residual sensitivity of the sensor to detect unwanted wavelengths including visible light that is “redder” than ultraviolet (Budzien et al., 2019). The main scientific objectives of IPM are follows: (1) Measure 135.6 nm emission in the night-side thermosphere to capture the large-scale structure of the low- and mid-latitude ionosphere. (2) Measure 135.6 nm and N<sub>2</sub> LBH emissions in the day-side thermosphere to capture global variations O/N<sub>2</sub> ratio and evolutions of the thermosphere and ionosphere during extreme space weather events. The FY3D is an afternoon sun-synchronous satellite with an orbit altitude of 830 km, an inclination of 98.75 °and orbit period of ~102 minutes, and is designed for weather forecast, atmospheric chemistry, climate change monitoring, and space weather monitoring. The FY3D satellite was launched at 18:35 UTC on November 14, 2017 from the Taiyuan Satellite Base, Shanxi province, China. This paper presents instrumental descriptions and initial observations by IPM.

## 2 Instrument Description

### 2.1 Instrument parameters requirements

60 | According to the two main scientific objectives mentioned above, the IPM instrument ~~parameters~~ requirements are summarized in the Table1. In the design of the ionospheric photometer, there are two important problems to be solved. One problem is red-leak. It is a major challenge to ionospheric photometers that visible light radiation from the sun is about 109 times more than FUV radiation. The other problem is that ionospheric photometers need to eliminate 130.44nm and shorter wavelengths airglow and collect 135.6 nm airglow emission with high sensitivity.

Table 1. FY-3D IPM instrument ~~parameters~~ requirements.

Parameter	value
Wavelength	135.6 nm (night mode)
	135.6 nm and 145-180nm (day mode)
Field of View	~3.5 °(along orbit)×1.6 °(cross orbit)
Sensitivity	day mode: ≥1 counts/s/Rayleigh@135.6nm
	night mode: ≥150 counts/s/Rayleigh@135.6nm
Spatial resolution	~30km@ionosphere (300km)
Time resolution	2 s (day mode)
	10 s (night mode)

65

## 2.2 Composition, channel, and mode

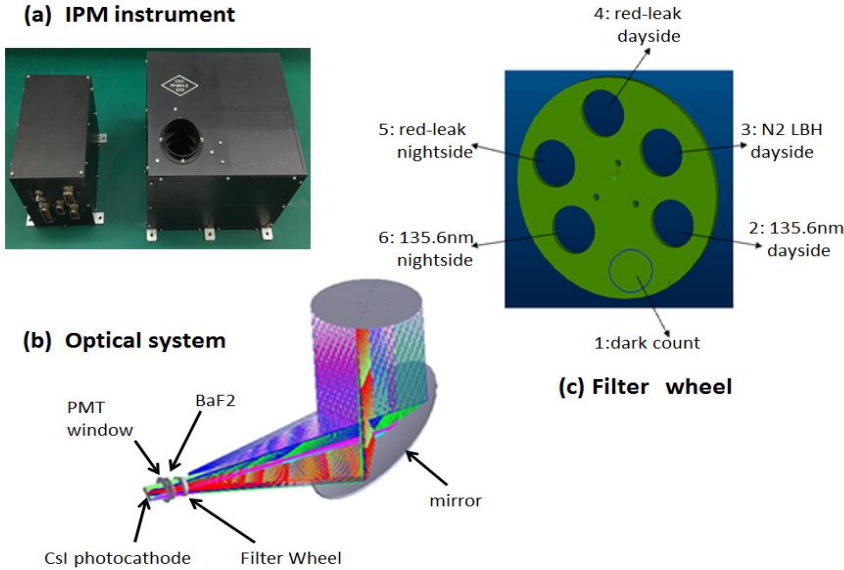


Figure 1: IPM instrument.

70

The IPM instrument is shown in Fig. 1 and includes a telescope, a filter wheel, a detector system, and control electronics cabinet. The telescope has a field-of-view of  $3.5^\circ$  (along orbit)  $\times$   $1.6^\circ$  (cross orbit). An off-axis aluminum mirror coating  $\text{MgF}_2$  is used to collect airglow emission in the telescope. To suppress the longer wavelength radiance, a sunblind PMT (R10825, Hamamatsu) with CsI photocathode is used in the detector system (Fu et al, 2015). The quantum efficiency of the PMT with an effective area of  $4 \times 9.5 \text{ mm}$ , is about 26 % at the wavelength 135.6 nm,  $6.17 \times 10^{-5}$  at 254 nm, and  $4.06 \times 10^{-8}$  at 514 nm. The PMT has better than  $10^{-4}$  rejection at wavelengths longer than 200 nm.

75

IPM monitors 135.6 nm emissions in the nighttime and 135.6 nm and  $\text{N}_2\text{LBH}$  emissions in the daytime by employing a filter wheel. There are six spots in the filter wheel (Fig. 1 (c)) corresponding to six channels of IPM: dark count channel, 135.6 nm nightside channel, red-leak nightside channel, red-leak dayside channel,  $\text{N}_2\text{LBH}$  dayside channel, and 135.6 nm dayside channel. The Channel information of IPM is shown in Table 2. In order to suppress the longer wavelength radiance further, the band-pass filter centred on 135.6 nm is used in the 135.6 nm dayside channel, and the band-pass filter centred on 160 nm is used in the  $\text{N}_2\text{LBH}$  channel. Besides, IPM specifically adds two red-leak signal channels for daytime and nighttime red-leak respectively. Based on the design of dayside or nightside channel, a  $\text{SiO}_2$  filter is added in the red-leak channels in order

80

to eliminate ~~below longer than~~ 180 nm ~~wavelength airglow~~. By differencing the measurements of dayglow channels and red-leak dayside channel, dayglow radiations can be detected. And by differencing the measurements of 135.6 nm nightside channel and red-leak nightside channel, 135.6 nm radiation in the nighttime can be detected. To exclude radiation shorter than 135.6 nm completely, a 0.5 mm-thin VUV-grade BaF<sub>2</sub> flat filter is used and the transmittance at 135.6 nm at room temperature is 0.5 (Fu et al., 2015). The emission of wavelengths shorter than 132 nm cannot pass the 0.5 mm-thick BaF<sub>2</sub> filter over a temperature range of 5 °C to 35 °C.

Table2. Channel information.

Number	Name	Filter
1	dark count channel	none
2	135.6nm dayside channel	BaF <sub>2</sub> +bandpass
3	N <sub>2</sub> LBH dayside channel	BaF <sub>2</sub> +bandpass
4	red-leak dayside channel	BaF <sub>2</sub> +bandpass+quartz
5	red-leak nightside channel	BaF <sub>2</sub> +quartz
6	135.6nm nightside channel	BaF <sub>2</sub>

带格式的: 下标

IPM has two observation modes: day mode and night mode. The day mode includes 4 ~~times~~ observations of the 135.6 nm dayside channel, 4 ~~times~~ observations of the N<sub>2</sub> LBH channel, 2 ~~times~~ observations of the red-leak dayside channel, and 1 dark count observation in each frame. The night mode includes 8 ~~times~~ observations of the 135.6 nm night channel, 1 observation of the red-leak nightside channel, and 1 dark count observation.

### 2.3 Laboratory Calibration

The IPM was calibrated in ground laboratory prior to flight. The optical calibration facility in ~~ground the ground laboratory~~ has a deuterium lamp, a monochromator, a collimator, a diffuser ~~board, and~~ a NIST standard detector ~~and a vacuum chamber~~ assembled in a modular pattern (Fig. 2). The deuterium lamp (L11798) with a MgF<sub>2</sub> window has 150W power and provides a bright, stable source of FUV radiation. The source of FUV radiation is wavelength-selected by the monochromator (234/302) which has a *f*/4.5 0.2 m Czerny-Turner with a 1200 grooves/mm grating. A collimator ensures that the beam consists of parallel rays. The NIST standard detector (AXUV-100G) ~~traced from NIST~~ provides a reference for calibrating IPM. ~~The entire facility is installed in a vacuum environment which allows the propagation of radiation in the far ultraviolet.~~

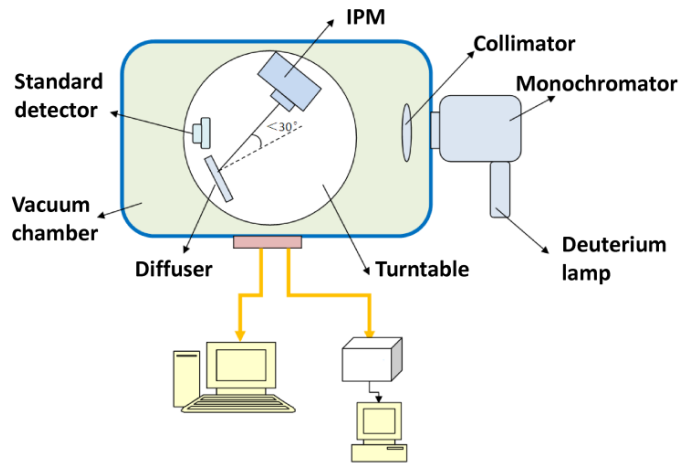


**Figure 2: The optical calibration facility in ground**

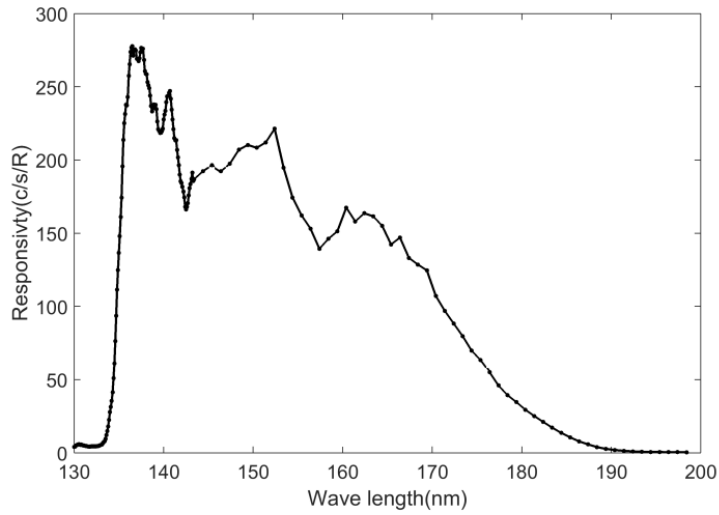
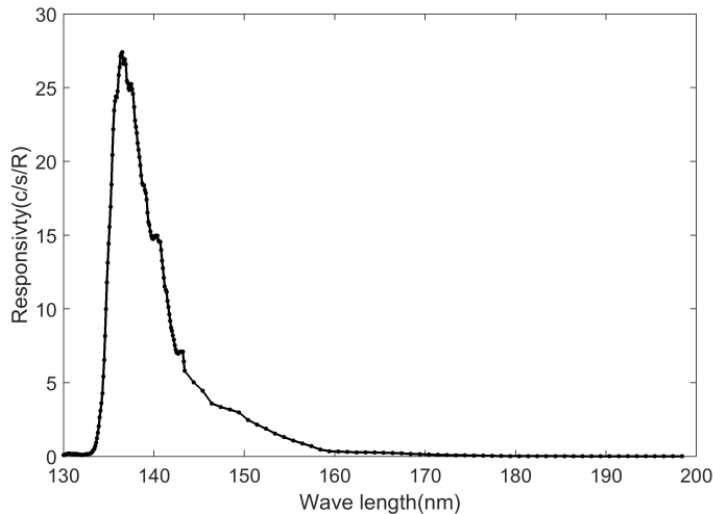


**Figure 23: The IPM responsivity of the 135.6nm nightside channel in counts/s/R.**

110

The processes of calibration are following: First, the FUV light at 125-200 nm from a the deuterium lamp is selected by the monochromator. Second, the wavelength-selected light reaches the NIST standard detector through the collimator, and the

115 NIST standard detector obtains the irradiance of the wavelength-selected-light. And then, by using a rotating platform, the  
wavelength-selected-light reaches the diffuser board through the collimator and enters IPM. IPM obtains the count-of-signal  
for the wavelength-selected-light. Finally, the count and irradiance of the wavelength-selected-light are used in calculating  
the responsivity to the wavelength-selected-light. The uncertainty of the ground calibration comes from the stability of the  
FUV light source, the error of the standard detector, the bi-directional reflection distribution function (BRDF) uncertainty of  
120 the diffuser board, the non-uniformity of the light source, and so on. The uncertainty of the ground calibration is estimated to  
reach 11.25%. As a function of wavelength, the responsivity of the 135.6 nm nightside channel from 130 to 200 nm is shown  
in Figure 23. The responsivity to 135.6 nm radiation at night is about 266.9 counts/s/R near the peak of the responsivity  
function distribution, and reaches the design requirement of the 135.6 nm nightside channel. The responsivity to 135.6 nm  
radiation at night provides high sensitivity in observations of OI 135.6 nm radiation at night.



125 **Figure 34: The IPM responsivity of the 135.6nm dayside channel in counts/s/R.**

130 As a function of wavelength, the responsivity of the 135.6 nm dayside channel from 130 nm to 200 nm is shown in Figure 34.  
The responsivity to the 135.6 nm radiation in daytime is about 23.20 counts/s/R, and also reaches the design requirement of  
the 135.6 nm dayside channel. The responsivity is much less than the one on the nightside due to the bandpass used in the  
135.6 nm dayside channel, which is designed to obtain the radiation of 135.6 nm in daytime and suppress the radiation at  
wavelengths shorter than 135.6 nm, N<sub>2</sub> LBH and red-leak contributions in daytime. The other bandpass is used in the N<sub>2</sub>

LBH day channel in order to obtain the radiation of N<sub>2</sub> LBH and suppress the radiation of 135.6 nm and red-leak contributions in daytime. The responsivity of N<sub>2</sub> LBH channel is shown in Figure 45.

135

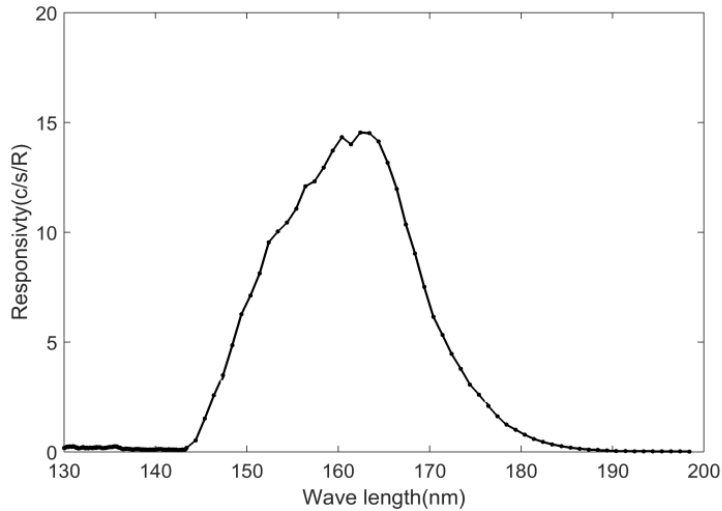


Figure 45: The IPM responsivity of the N<sub>2</sub> LBH channel in counts/s/R.

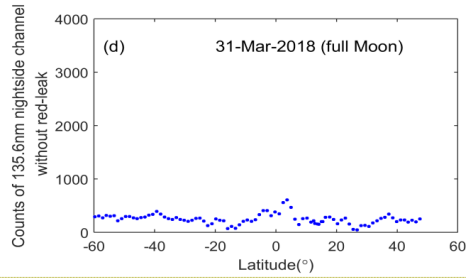
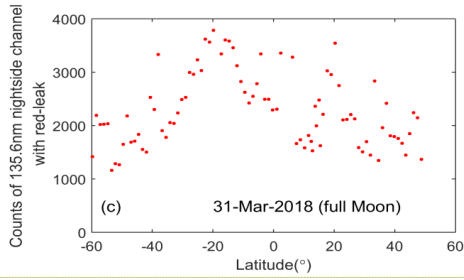
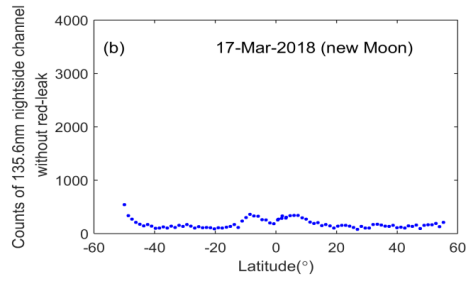
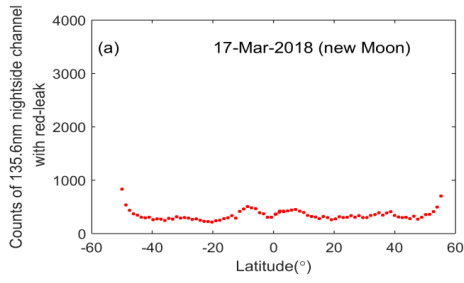
### 3 Observation Results

#### 140 3.1 OI 135.6 nm emission on the nightside

After the FY3D satellite was launched at 18:35 UTC on November 14, 2017, IPM started operation at 10:20 UTC on November 25, 2017. In IPM data processing, dark count is used to confirm the working status of IPM. Generally, the dark count of IPM is less than 10 counts per second. When the FY3D satellite passes by the South Atlantic Anomaly (SAA), the dark count of IPM increases rapidly and reaches ~~a peak~~ about 2000 counts per second due to the ~~high~~ energetic particles ~~over~~ in the SAA.

145





**带格式的:** 字体: (中文) +中文正文  
(宋体), 8 磅, 加粗

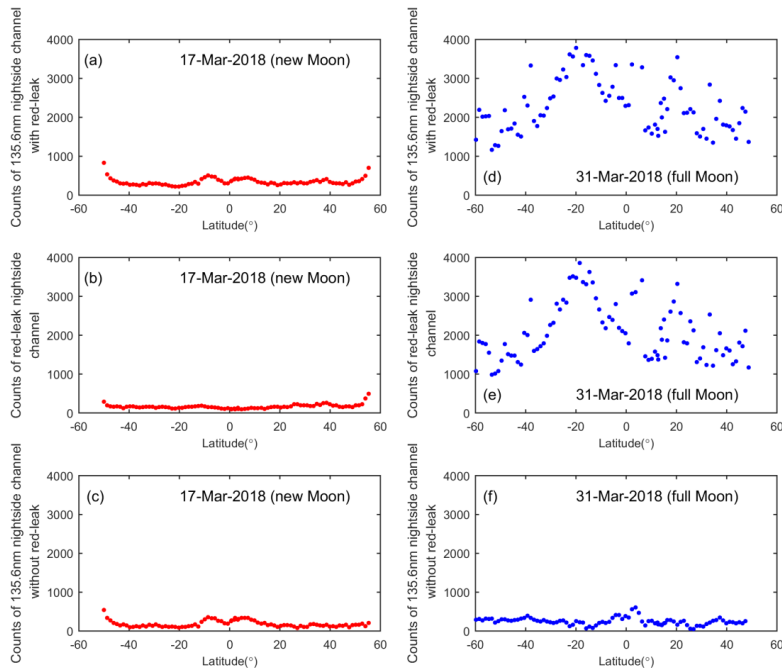


**Figure 6: The count of the 135.6nm nightside channel with red-leak (top), without red-leak (bottom), and the count of the red-leak nightside channel (middle) for new Moon (left) and full Moon (right) situation, respectively. March 17, 2018 is new Moon day, and March 31, 2018 is full Moon day. Figure 5: The count of the 135.6nm nightside channel with (left) and without (right) red-leak for new Moon (top) and full Moon (bottom) situation, respectively. March 17, 2018 is new Moon day, and March 31, 2018 is full Moon day.**

150

155

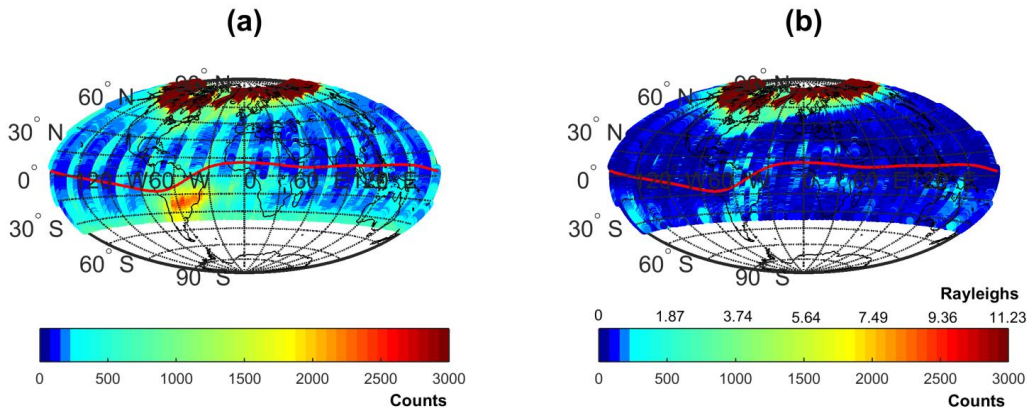
160

The count of the 135.6 nm nightside channel is presented in Fig. 56. The count with red-leak on March 17, 2018 (new Moon) and on March 31, 2018 (full Moon) are shown in (a) and (ed), respectively. The count without red-leak on March 17, 2018 and March 3, 2018 are shown in (bc) and (df), respectively, ~~which deducted the count of red-leak~~. The count of the 135.6 nm nightside channel in (ed) is several times the count of the 135.6 nm nightside channel in (a) due to moonlight reflecting into the 135.6 nm nightside channel from cloud tops, while the count levels in (bc) and (df) are very similar. We found that the red-leak nightside channel is effective to ~~deduct-eliminate~~ the contamination of moonlight on the 135.6 nm nightside channel. ~~The An~~ example of the global count of the 135.6 nm nightside channel is presented in Fig. 6-7 (a). The red solid line indicates the magnetic dip equator. The data in Fig. 6-7 are from 7 to 11 December 2017. From 7 to 11 December 2017, Kp

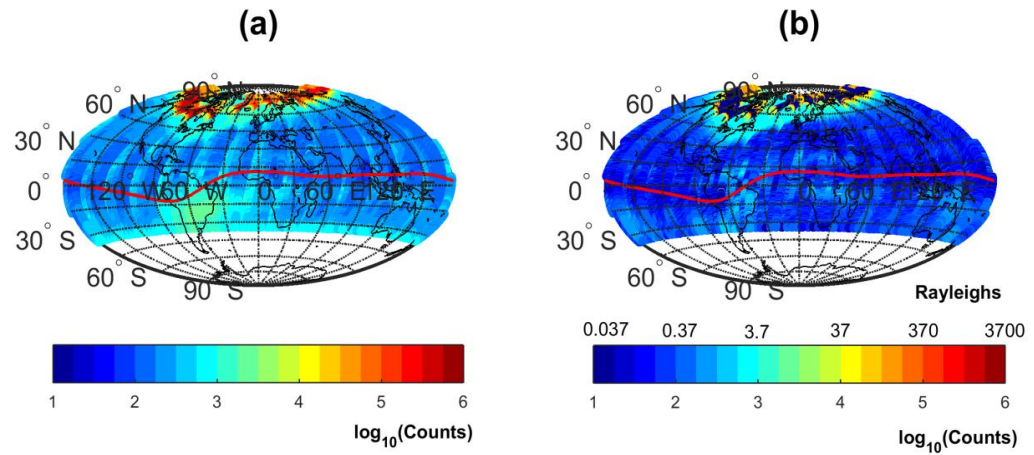
index is not more than 4 and the geomagnetic conditions kept quiet was relatively quite. As shown in Fig. 6 (a), there is a high-count area near the magnetic dip equator in South America, which shows the contamination in SAA associated with particles impacting the instrument. The An example of global brightness of the 135.6 nm nightside channel without red-leak and the effect of dark count is presented in Fig. 6-7 (b). As shown Fig. 6-7 (b), there are some brighter areas located on either side of the magnetic dip equator in South America and Africa, which are the so-called equatorial ionization anomaly (EIA) structure. The EIA has been

165

170



带格式的: 字体: (中文) +中文正文 (宋体), 8 磅, 加粗



带格式的: 居中  
带格式的: 英语(美国)

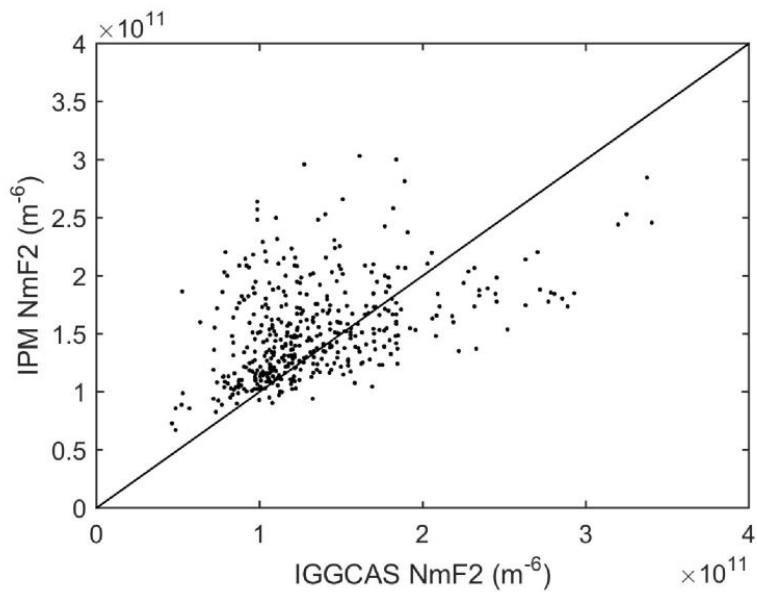
**Figure 67: The global count (left) and brightness (right) of the 135.6nm nightside channel from 7 to 11 December 2017. The brightness is without red-leak and the effect of dark count. The red solid line indicates the magnetic dip equator.**

175 studied extensively by using data from ground-based ionosodes (Moffett and Hanson, 1965; Walker, 1981) and ground-  
based optical observations (Thuillier et al., 1976). The OI 135.6 nm emission data from GUVI on board TIMED satellite,  
180 FUV on board the IMAGE satellite, and the TIP on board the COSMIC satellites have also been used in study of the EIA  
phenomenon (Christensen et al., 2003; Sagawa et al., 2005; Immel et al, 2006 and Coker et al., 2009). The local time of the  
IPM orbit on the nightside is 2:00 am. The EIA structure which we found at the 2:00 local time is later than other results  
mentioned earlier, and it need to be studied furtherly.

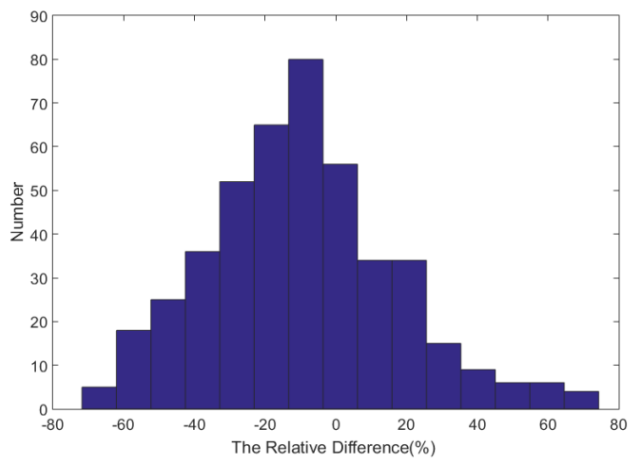
### 3.2 NmF<sub>2</sub> and TEC

OI 135.6 nm emission is one of the strongest lines in the FUV nightglow at low latitudes and has relatively high transparency  
in the upper atmosphere. In the nightside ionosphere, there are two primary production mechanisms of OI 135.6 nm emission:  
185 (1) Atomic oxygen is excited through the recombination of atomic oxygen ions with electrons and produces OI 135.6 nm  
emission; (2) Atomic oxygen is excited through the mutual neutralization of O<sup>+</sup> with O<sup>-</sup> and produces OI 135.6 nm emission  
(Meier, 1991). The mutual neutralization has a relatively smaller contribution. The brightness of OI 135.6 nm emission  
varies with the electron density and the oxygen ion concentration basically. Equivalently, OI 135.6 nm emission is  
approximately proportional to the square of the electron density in the F-region.

The algorithm of deriving NmF<sub>2</sub> from the night time OI 135.6 nm emission is provided by Rajesh et al. (2011) and Jiang et  
190 al. (2014, 2018). The night time OI 135.6 nm emission is calculated based on nighttime OI 135.6 nm airglow radiative and  
emissive model. The electron density profile, the O<sup>+</sup> density profile, and the electron temperature profile are calculated  
using IRI2000 model, and the neutral components are calculated using MSISE90 model. The OI 135.6 nm emission is  
fitted to the square of NmF<sub>2</sub> linearly. The ratio of the square of NmF<sub>2</sub> to the OI 135.6 nm emission is obtained. Finally,  
NmF<sub>2</sub> is retrieved based on the observed OI 135.6 nm emission and the ratio.~~Based on the previous studies of the nighttime  
195 OI 135.6 nm airglow using the radiative and emissive model, IRI2000 model, and MSISE90 model, the retrieval algorithm of  
NmF<sub>2</sub> derived from nighttime OI 135.6 nm emission was presented by Jiang et al. (2018). The brightness of the nighttime OI  
135.6 nm emission is used to calculate ionospheric NmF<sub>2</sub> by the ratio between NmF<sub>2</sub> and OI 135.6 nm emission from the  
retrieval algorithm.~~ We selected the IPM derived NmF<sub>2</sub> data which were near to four IGGCAS ionosonde stations(Sanya  
(18.3 °N,109.6 °E), Wuhan (30.5 °N,114.4 °E), Beijing (40.3 °N,116.2 °E), and Mohe (50.2 °N,122.5 °E)) from November 25,  
200 2017 to May 8, 2018(shown in Fig. 8). Their difference in longitude ~~were~~ less than 12 °and in latitude ~~were~~ less  
than 5 °. There is a standard deviation of 26.67% between IPM NmF<sub>2</sub> and IGGCAS ionosonde NmF<sub>2</sub> (shown in Fig. 79).



205 **Figure 28:** IPM derived NmF<sub>2</sub> and IGGCAS ionosondes NmF<sub>2</sub> from November 25, 2017 to May 8, 2018. (The longitude difference between the IPM substellar point and ionosonde stations is less than 12 °; and the latitude difference is less than 5 °.)



带格式的: 居中

**Figure 9: The relative difference distribution between IPM NmF<sub>2</sub> and IGGCAS ionosonde NmF<sub>2</sub>.**

210 ~~The algorithm of deriving TEC from the night time OI 135.6 nm emission is provided by Rajesh et al. (2011) and Jiang et al. (2014). The process of deriving TEC based on the ratio between TEC and the night time OI 135.6 nm emission intensity is similar to that of deriving NmF<sub>2</sub> (2014).~~ We further calculated total electron content (TEC) from IPM results and compared with that of MIT TEC data from November 25, 2017 to April 8, 2018. The MIT TEC data (Rideout and Coster, 2006) was obtained from the MIT Haystack Observatory Madrigal database (<http://www.openmadrigal.org>). There is a standard deviation of 39.41% between IPM TEC (total electron content unit, TECu) and MIT TEC (TECu) (shown in Fig. 810). The standard deviation between IPM TEC (TECu) and MIT TEC (TECu) is more than the one between IPM NmF<sub>2</sub> and IGGCAS ionosonde NmF<sub>2</sub>. ~~MIT TEC is intergraded from ground to 20200Km. It includes plasmasphere contribution and ionosphere contribution. IPM TEC is intergraded from ground to 830Km, it only includes ionosphere contribution. In the Ionosphere plasmasphere coupled system, the ionosphere in conjugate hemispheres forms a plasmasphere reservoir along the interconnecting flux tube.~~ There is diurnal interchange between the ionosphere and the plasmasphere, ~~the downward diffusion from the plasmasphere helps to maintain the nighttime F<sub>2</sub>-layer. that the downward diffusion from the plasmasphere helps to maintain the nighttime F<sub>2</sub>-layer.~~ The results of Jason-1, Metop-A, and TerraSAR-X (Yizengawa et al., 2008; Zakharenkova and Cherniak, 2015; Klimenko et al., 2015) show that ~~the plasmasphere contribution at night can't be neglected. at day the contribution of the plasmasphere in TEC is less than the one of the ionosphere, whereas at night the contribution of the plasmasphere in TEC is increasing and even more than the one of the ionosphere.~~

220

225

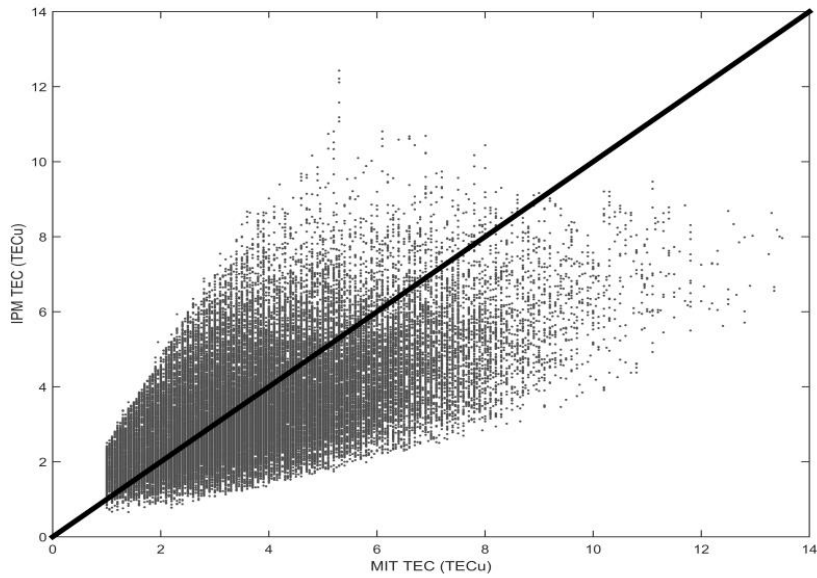
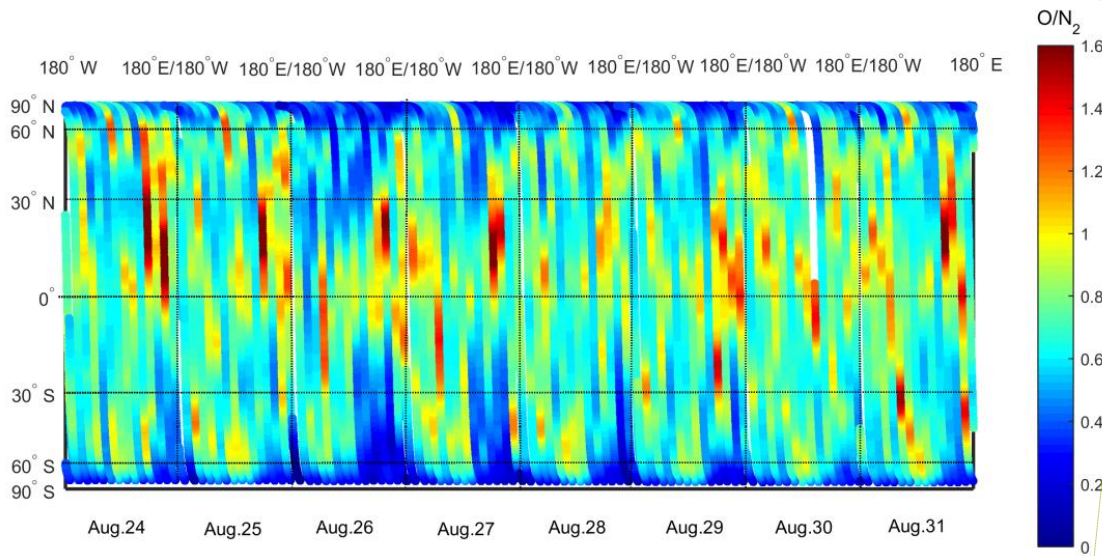


Figure 810: IPM TEC and MIT TEC (TECu) from November 25, 2017 to April 8, 2018

230

Auroral emission can be derived from the 135.6 nm nightside channel. There is obviously a strong auroral emission feature in the Northern Hemisphere in Fig. 6. By the way, the wide field auroral imager (WAI), one of ten scientific instruments aboard the Feng Yun 3D meteorological satellite, has provided large field of view (FOV), high spatial resolution, and broadband ultraviolet images of the aurora (Zhang et al., 2019).

### 3.3 O/N<sub>2</sub>



带格式的: 字体: 8 磅

235

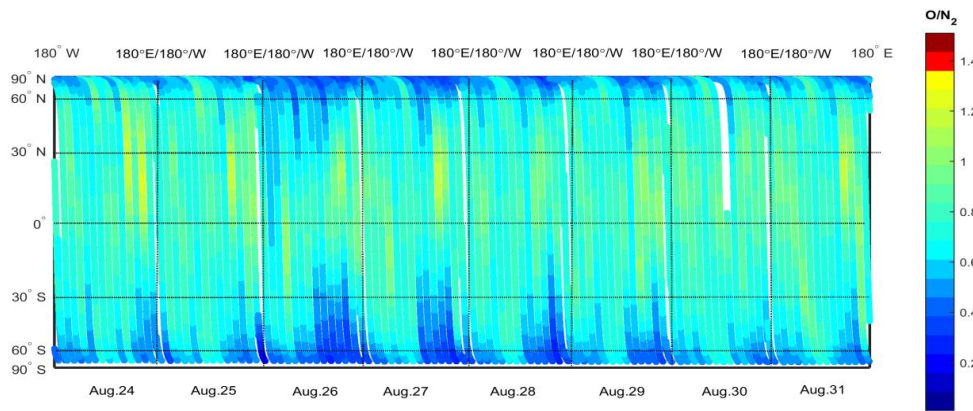


Figure 911: Column O/N<sub>2</sub> from IPM around the magnetic storm of Aug.26, 2018.

240

Energetic photon-electron impact excitation of the neutral atmosphere produces 135.6 nm emission and N<sub>2</sub>LBH emission, which are proportional to the concentration of O and N<sub>2</sub> respectively (Meier, 1991). 135.6 nm emission and N<sub>2</sub>LBH



emission can be used to derive column O/N<sub>2</sub>. The derivation of O/N<sub>2</sub> from disk 135.6 and N<sub>2</sub>LBH dayglow observations was first addressed by Strickland et al. (Strickland et al., 1995) And the topic of O/N<sub>2</sub> from 135.6 nm emission and N<sub>2</sub>LBH emission has been studied extensively (Christensen et al., 2014; Strickland et al., 2004; Zhang et al., 2014). During geomagnetic storms enhanced Joule and particle heating in the high latitude ionosphere produces upwelling of the oxygen-depleted or nitrogen-rich air. The upwelling rises from much lower in the thermosphere into the F region. The heating also leads to enhanced horizontal equator-ward neutral winds that can change the distribution of the nitrogen-rich/oxygen-depleted air.

245 ~~Giving an N<sub>2</sub> depth of 10<sup>17</sup> cm<sup>-2</sup>, column O and N<sub>2</sub> ratio is derived from the value of at a given Solar Zenith Angle (SZA) by two-dimensional interpolation. The retrieval algorithm could refer in relevant paper (Strickland et al., 1995; Zhang et al., 2004). The brightness of 135.6 nm emission and N<sub>2</sub> LBH emission on dayside were derived from observations of the 135.6 nm dayside channel and the N<sub>2</sub> LBH dayside channel respectively. In order to further deducting the red-leak from the cloud tops, we used a Butterworth filter in data processing. The improved AURIC model (Wang and Wang, 2016) was used to produce a simulation. The simulation provided the coefficient of deriving O/N<sub>2</sub> from a measured pair of 135.6 and LBH. The brightness of 135.6 nm emission on dayside can be derived from observations of the 135.6 nm dayside channel and the N<sub>2</sub>LBH dayside channel respectively. A Butterworth filter is used in data processing in order to deduct the red leak from the cloud top. The simulation produced by the AURIC model (Wang and Wang, 2015) is used to obtain a lookup table that provides the coefficient of deriving O/N<sub>2</sub> from a measured pair of 135.6 and LBHS values. The result of column O and N<sub>2</sub> ratio during the magnetic storm of Aug. 26, 2018 is presented in Fig. 911. On 24 August 2018 and most of 25 August 2018, Kp index is-was not more than 3. It abruptly rises-rose 7 in 26 August 2018, descends and rises to 6 on 27 August 2018.~~

250 ~~The brightness of 135.6 nm emission on dayside can be derived from observations of the 135.6 nm dayside channel and the N<sub>2</sub>LBH dayside channel respectively. A Butterworth filter is used in data processing in order to deduct the red leak from the cloud top. The simulation produced by the AURIC model (Wang and Wang, 2015) is used to obtain a lookup table that provides the coefficient of deriving O/N<sub>2</sub> from a measured pair of 135.6 and LBHS values. The result of column O and N<sub>2</sub> ratio during the magnetic storm of Aug. 26, 2018 is presented in Fig. 911. On 24 August 2018 and most of 25 August 2018, Kp index is-was not more than 3. It abruptly rises-rose 7 in 26 August 2018, descends and rises to 6 on 27 August 2018.~~

255 ~~From 29 to 31 August 2018, Kp index is-was not more than 3. The column O/N<sub>2</sub> on 24 and 25 August is-was relatively quiet, and significant changes in column O/N<sub>2</sub> occur-red on 26 and 27 August. The reduction of O/N<sub>2</sub> extend-ed from the high-latitude region to mid and low latitude regions in the Northern and Southern Hemisphere. On 30 and 31 August, column O/N<sub>2</sub> returns-returned to quiet, to the level before the magnetic storm.~~

260 ~~From 29 to 31 August 2018, Kp index is-was not more than 3. The column O/N<sub>2</sub> on 24 and 25 August is-was relatively quiet, and significant changes in column O/N<sub>2</sub> occur-red on 26 and 27 August. The reduction of O/N<sub>2</sub> extend-ed from the high-latitude region to mid and low latitude regions in the Northern and Southern Hemisphere. On 30 and 31 August, column O/N<sub>2</sub> returns-returned to quiet, to the level before the magnetic storm.~~

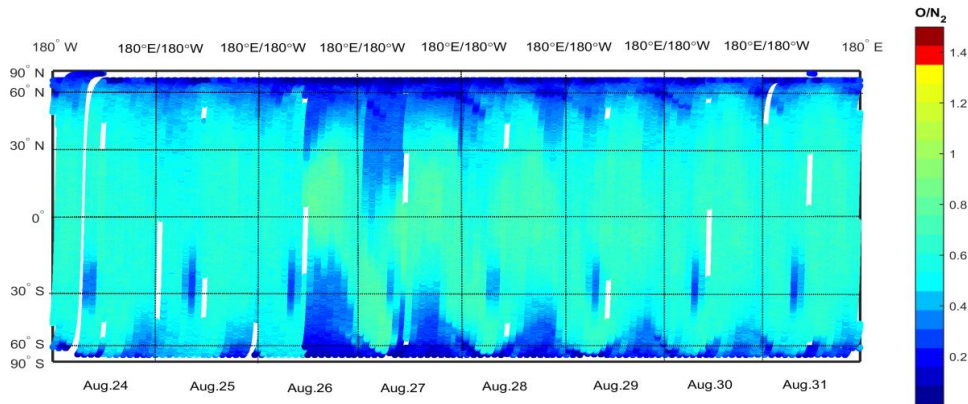


**Figure 12: Column  $O/N_2$  from GUVI around the magnetic storm of Aug.26, 2018.**

The column O and  $N_2$  ratio derived from GUVI during the magnetic storm of Aug. 26, 2018 is presented in Fig. 12. The GUVI column  $O/N_2$  data (Strickland et al., 2004) was obtained from GUVI website ([http://guvitimed.jhuapl.edu/data\\_fetch\\_13\\_on2\\_idlsave](http://guvitimed.jhuapl.edu/data_fetch_13_on2_idlsave)). The column  $O/N_2$  from GUVI on 24 and 25 August was relatively quiet, and significant changes in column  $O/N_2$  occurred on 26 and 27 August. The reduction of  $O/N_2$  also extended from the high-latitude region to mid- and low-latitude regions in the Northern and Southern Hemisphere. On 30 and 31 August, the column  $O/N_2$  of GUVI also returned to quiet. The features of column  $O/N_2$  of IPM and GUVI during the magnetic storm of Aug. 26, 2018 were similar. These results showed that the IPM data could provide a good monitoring of  $O/N_2$  changes during the magnetic storm.

#### 4 Conclusion

The Feng Yun 3D (FY3D) meteorological satellite was launched at 18:35 UTC on November 14, 2017 from the Taiyuan Satellite Base, Shanxi province, China. The Ionospheric Photometer instrument carried aboard the FY3D Feng Yun 3D meteorological satellite measures the spectral radiance of the Earth far ultraviolet airglow in the spectral region from 133 to 180 nm. IPM is a tiny, highly sensitive, and robust remote sensing instrument. Preliminary observations show that the IPM could monitor the global structure of the equatorial ionization anomaly structure around 2:00 local time using OI 135.6 nm nightglow properly. It could also identify the reduction of  $O/N_2$  in the high-latitude region during the geomagnetic storm of Aug. 26, 2018. The IPM derived  $NmF_2$  accords well with that observed by 4 ionosonde stations along 120°E with a standard deviation of 26.67%. Initial results demonstrate that the performance of IPM meets the designed requirements, and therefore can be used to study the thermosphere and ionosphere in future.

*Data availability.* Data are available at <http://satellite.nsmc.org.cn/PortalSite/Default.aspx>.

285

*Author contributions.* Yungang Wang and Tian Mao performed the data validation and prepared the paper and most of the plots; Liping Fu and Fang Jiang designed IPM and provided laboratory calibration data; Xiuqing Hu, Chengbao Liu, Xiaoxin Zhang, Jiawei Li, Ling Sun, Zhongdong Yang, Peng Zhang and Jingsong Wang participated in instrument parameters requirements, judging of instrument design and data validation; Zhipeng Ren, Fei He and Lingfeng Sun participated in validation and intercomparisons.

290

*Competing interests.* The authors declare that they have no conflict of interest.

*Financial support.* This research has been supported by the Natural Science Foundation of China under Grant 41874187, 41774195, and 41931073 and Fengyun Satellite Ground Application System.

295

## References

Anthes, R. A., Bernhardt, P. A., Chen, Y., Cucurull, L., Dymond, K. F., Ector, D., Healy, S. B., Ho, S., Hunt D. C, Kuo, Y., Liu, H., Maning, K., McCormick, C., Meehan, T. K., Randel, W J., Rocken, C., Schreiner, W S., Sokolovskiy, S. V., Syndergaard, S., Thompson, D. C., Trenberth, K.E., Wee, T., Yen, N. L., and Zeng, Z.: The COSMIC/FORMOSAT-3 mission: early results, *Bull. Am. Meteor. Soc.* vol.89, 313–333, doi:10.1175/BAMS-89-3-313 , 2008.

300

Budzien, S., Fritz, B., Stephan, A., Marquis, P., Powell, S., O’Hanlon, B., Nicholas, A., Dymond, K., and Brown, C.: Comparison of second and third generation 135.6 nm ionospheric photometers using onorbitand laboratory results , *CubeSats and SmallSats for Remote Sensing III*, International Society for Optics and Photonics, SPIE, 1–13, doi:10.1117/12.2528791, 2019.

305

Budzien, S., Powell, S., O’Hanlon, B., Bishop, R., Humphreys, T., Stephan, A.: Early Results and Ionospheric Observations from GROUP-C on the ISS, 15th International Ionospheric Effects Symposium, Alexandria, Virginia, Paper 11A3, 2017.

Christensen, A. B., Paxton, L. J., Avery, S., Craven, J., Crowley, G., Humm, D. C., Kill, H., Mejer, R. R., Meng, C., Morrison, D., Ogorzalek, B. S., Straus, P., Strickland, D. J., Swenson, R. M., Walterscheid, R. L., Wolven, B., and Zhang, Y.: Initial observations with the Global Ultraviolet Imager (GUVI) in the NASA TIMED satellite mission, *J. Geophys. Res.*, vol.108, no.A12, 1-16, doi:10.1029/2003JA009918, 2003.

310

Coker, C., Dymond, K. F., Budzien, S. A., Chua, D. H., Liu, J., Anderson, D. N., Basu, S., and Pedersen, T. R.: Observations of the ionosphere using the tiny ionospheric photometer, *Terr. Atmos. Ocean. Sci.*, vol.20, no.1, 227–235, doi:10.3319/TAO.2008.01.18.02 (F3C), 2009.

315

Dymond, K. F., Budzen, S. A., Coker, C., and Chua, D. H.: The Tiny Ionospheric Photometer (TIP) on the Constellation

- Observing System for Meteorology, Ionosphere, and Climate (COSMIC/FORMOSAT-3), *J. Geophys. Res. Space Physics*, vol.121, 10, 614–10,622, doi:10.1002/2016JA022900, 2016.
- Dymond, K. F., Nicholas, A. C., Budzien, S. A., Stephan, A. W., Marquis, P., Brown, C. M., Finne, T., and Wolfram, K. D.: Low-latitude ionospheric research using the CIRCE Mission: instrumentation overview, UV, X-Ray, and Gamma-Ray Space Instrumentation for Astronomy XX, Proc. SPIE 10397, 1039719, 2017.
- Fu, L., Peng, R., Shi, E., Peng, J., Wang, T., Jiang, F., Jia, N., Li, X., and Wang, Y.: Far Ultraviolet nighttime ionospheric photometer, *Astrophys Space Sci.*, vol.355, no.1, 1-7, doi: 10.1007/S10509-014-2139-9, 2015.
- [Huffman, R. E., Leblanc, F. J., Larrabee, J. C. and Paulsen, D. E.: Satellite vacuum ultraviolet airglow and auroral observations, \*J. Geophys. Res.\*, vol.85, no.A5, 2201-2215, doi: 10.1029/JA085iA05p02201, 1980.](#)
- [Immel, T. J., Sagawa, E., England, S. L., Henderson, S. B., Hagan, M. E., Mende, S. B., Frey, H. U., Swenson C. M., and Paxton, L. J.: Control of equatorial ionospheric morphology by atmospheric tides, \*Geophys. Res. Lett.\*, vol.33, L15108, 1-4, doi:10.1029/2006GL026161, 2006.](#)
- Jiang, F., Mao, T., and Fu, L.: The research on NmF<sub>2</sub> and TEC derived from nighttime OI 135.6 nm emission measurement, *Chinese J. Geophys.* (in Chinese), vol.57, no.11, 3679-3687, doi:10.6038/cjg20141122, 2014.
- Jiang, F., Mao, T., Li, X., Fu, L., Wang, Y., and Yu, T.: Retrieval algorithm and precision analysis for NmF<sub>2</sub> of nighttime OI 135.6 nm emission, *Chin. J. Space Sci.*, vol.38, no.1, 58-64, 2018.
- Klimenko, M. V., Klimenko, V. V., Zakharenkova, I. E., and Cherniak L. V.: The global morphology of the plasmaspheric electron content during northern winter 2009 based on GPS/COSMIC observation and GSM TIP model results, *Adv. Space Res.*, vol.55, no.8, 2077–2085, 2015.
- Meier, R. R.: Ultraviolet spectroscopy and remote sensing of the upper atmosphere, *Space Sci. Rev.*, vol.58, no.1, 1-185, doi:10.1007/BF01206000, 1991.
- [Immel, T. J., Sagawa, E., England, S. L., Henderson, S. B., Hagan, M. E., Mende, S. B., Frey, H. U., Swenson C. M., and Paxton, L. J.: Control of equatorial ionospheric morphology by atmospheric tides, \*Geophys. Res. Lett.\*, vol.33, L15108, 1-4, doi:10.1029/2006GL026161, 2006.](#)
- Moffett, R. J. and Hanson, W. B.: Effect of ionization transport on the equatorial F-region, *Nature*, vol.206, no.4985, 705-706, 1965.
- Paxton, L. J., Morrison, D., Strickland, D. J., McHarg, M. G., Zhang, Y.L., Wolven, B., Kill, H., Crowley, G., Christensen, A. B., and Meng, C.: The use of far ultraviolet remote sensing to monitor space weather, *Adv. Space Res.*, vol.31, no.4, 813-818, doi:10.1016/S0273-1177(02)00886-4, 2003.
- [Rajesh, P. K., Liu, J. Y., Hsu, M. L., Lin, C. H., Oyama, K. I. and Paxton, L. J.: Ionospheric electron content and NmF<sub>2</sub> from nighttime OI 135.6 nm intensity, \*J. Geophys. Res.\*, vol.116, A02313, 1-16, doi:10.1029/2010JA015686, 2011.](#)
- [Rideout, W., and Coster, A.: Automated GPS processing for global total electron content data, \*GPS Solutions\*, 10, 219–228, doi:10.1007/s10291-006-0029-5, 2006.](#)

- 350 | Sagawa, E., Immel, T. J., Frey, H. U., and Mende, S. B.: Longitudinal structure of the equatorial anomaly in the nighttime ionosphere observed by IMAGE/FUV, *J. Geophys. Res.*, vol.110, A11302, 1-10, doi:10.1029/2004JA010848, 2005.
- ~~Rideout, W., and Coster, A.: Automated GPS processing for global total electron content data, *GPS Solutions*, 10, 219–228, doi:10.1007/s10291-006-0029-5, 2006.~~
- 355 | Stephan, A. W., Marquis, P. J., Budzien, S. A., Dymond, K. F., Brown, C. M., Wolfram, K. D., and Nicholas, A. C.: Evaluation of UV optics for Triple Tiny Ionospheric Photometers on CubeSat missions: CubeSats and NanoSats for Remote Sensing, *Proc. SPIE*, 10769, 107690W, doi: 10.1117/12.2321042, 2018.
- Strickland, D. J., Evans, J. S., and Paxton, L. J.: Satellite remote sensing of thermospheric O/N<sub>2</sub> and solar EUV: 1, Theory, *J. Geophys. Res.*, vol.100, no.A7, 12217-12226, doi: 10.1029/95JA00574, 1995.
- 360 | Strickland, D. J., Meier, R. R., Walterscheid, R. L., Craven, J. D., Christensen, A. B., Paxton, L. J., Morrison, D., and Crowley, G.: Quiet-time seasonal behavior of the thermosphere seen in the far ultraviolet dayglow, *J. Geophys. Res.*, vol. 109, doi:10.1029/2003JA010220, 2004.
- Thuillier, G., King, J.W., and Slater, A. J.: An explanation of the longitudinal variation of the OI D (630 nm) tropical nightglow intensity, *J. Atmos. Terr. Phys.*, vol.38, no.2, 155-158, 1976.
- 365 | Walker, G.O.: Longitudinal structure of the F-region equatorial anomaly: a review, *J. Atmos. Terr. Phys.*, vol.43, no.8, 763-774, doi: 10.1016/0021-9169(81)90052-0, 1981.
- Wang, H. and Wang, Y.: Airglow simulation based on the atmospheric ultraviolet radiance integrated code of 2012, *Science China: Earth Sciences*, vol. ~~45~~59, ~~1768~~125–1780~~435~~, ~~2015~~2016.
- Yizengawa, E., Moldwin, M. B., Galvan, D., Lijima, B. A., Komjathy, A., and Mannucci, A. J.: Global plasmaspheric TEC and its relative contribution to GPS TEC, *J. Atmos. Terr. Phys.*, vol.70, 1541-1548, doi:10.1016/j.jastp.2008.04.022, 2008.
- 370 | Zakharenkova, I. and Cherniak, L.: How can GOCE and TerraSAR-X contribute to the topside ionosphere and plasmasphere research, *Space Weather*, vol.13, 271-285, doi:10.1002/2015SW001162, 2015.
- ~~Zhang, X., Chen, B., He, F., Song, K., He, L., Liu, S., Guo, Q., Li, J., Wang, X., Zhang, H., Wang, H., Han, Z., Sun, L., Zhang, P., Dai, S., Ding, G., Chen, L., Wang, Z., Shi, G., Yu, C., Yang, Z., Zhang, P., and Wang, J.: Wide field auroral imager onboard the Fengyun satellite, *Light: Science & Applications*, vol.8, no.47, 1-12, doi:10.1038/s41377-019-0157-7, 2019.~~
- 375 | Zhang, Y., Paxton, L. J., Morrison, D., Marsh, D., and Kil, H: Storm-time behaviors of O/N<sub>2</sub> and NO variations, *J. Atmos. Terr. Phys.*, vol.114, 42-49, doi:10.1016/j.jastp.2014.04.003, 2014.

380